Constraints on Magma Chamber Geometry at Sierra Negra Volcano, Galápagos Islands, based on InSAR Observations

S. Yun [a] and P. Segall [a] H. Zebker [a]

[a] *Department of Geophysics, Stanford University, Stanford, CA, 94305, USA*

Abstract

We investigate the problem of estimating magma chamber geometry using InSAR observations of Sierra Negra volcano, Galápagos. Ascending and descending interferograms are combined to determine vertical and one horizontal component of displacement. The ratio of maximum horizontal to vertical displacement suggests a sill-like source. Spherical or stock-like bodies are inconsistent with the data. We estimate the geometry of the sill assuming a horizontal, uniformly pressurized crack with unknown periphery and depth. The sill is discretized into small elements that either open, and are subjected to the pressure boundary condition, or remain closed. We find the best-fitting sill to be located beneath Sierra Negra's inner caldera at a depth of about 2 km. Using boundary element calculations we show that any magma chamber with a flat top coincident with the sill model fits the data equally well. The data are insensitive to the sides and bottom of the magma chamber.

Key words: Sierra Negra Volcano; Galápagos; Synthetic Aperture Radar Interferometry; boundary element method; modeling; magmatic processes; geodesy

1 Introduction

Six volcanoes in the western Galápagos islands of Fernandina and Isabela (Fig. 1) have been actively deforming since 1992 (Amelung et al., 2000). Among these Sierra Negra is by far the most voluminous and has been one of the most active. It has experienced 11 historical eruptions, including most recently the 0.9 km^3 eruption on the north flank of the volcano in 1979 (Reynolds et al., 1995). Sierra Negra's shallow caldera (110 m in maximum depth) is the largest by area in the western Galápagos (59.8 km^2) (Munro and Rowland, 1996). The caldera is characterized by a C-shaped sinuous ridge, composed of a complex set of normally faulted blocks with steep (60° - 90°) outward dipping fault scarps (Reynolds et al., 1995).

The center of Sierra Negra's caldera uplifted from 1992 to 1997, causing a line-of-sight (LOS) displacement of about 1.6 meters in InSAR observations (Amelung et al., 2000). The rapid inflation was followed by trapdoor faulting sometime in 1997-1998, which occurred along the pre-existing fault system inside the south moat of the caldera. This event was discovered using InSAR observations (Amelung et al., 2000). The faulting was also confirmed by field study and range offset measurements (Jónsson et al., in review 2004). The measured maximum slip along the fault plane was about 1.5 meters (Jónsson et al., in review 2004). After the trapdoor faulting event, Sierra Negra resumed uplift from September 1998 to March 1999 with a maximum LOS displacement of 30 cm. This uplift event was successfully modeled as a sill with spatially varying opening distribution by Amelung et al. (2000). A GPS network on Sierra Negra showed that subsidence initiated sometime between late 2000 and early 2001, at rates of up to 9 cm/yr (Geist et al., in review 2004).

In this paper, we reanalyze InSAR data, incorporating a more rigorous investigation of the geometry of the putative magma body. While we refer to the deformation source as a magma body, it may include a hydrothermal component. Although Amelung et al. (2000)'s sill model fits the observations very well, it does not prove that a sill is the only magma chamber geometry that can fit the data. It is well known that there is a non-uniqueness in the shape of plausible deformation sources given only vertical displacement data (Dieterich and Decker, 1975). Given vertical and horizontal displacement data, however, it is possible to distinguish sills from spherical chambers or stocks (Fialko et al., 2001a). Here we first constrain the shape of the magma chamber by reconstructing vertical and horizontal components of the surface displacement using two interferograms, one from an ascending orbit and the other from a descending orbit. This approach is similar to that of Fialko et al. (2001b) but does not require calculation of azimuth offsets because we need only two components to constrain the shape.

Amelung et al. (2000) allow the sill opening to vary spatially to fit the data, but did not impose any additional physical constraints on the shape. We explore below a new inversion approach, in which the deformation source is restricted to be a uniformly pressurized sill whose plan outline is unknown, appropriate for a magmatic intrusion. In this case the geometry of the sill and the magma pressure are the unknowns. Compared to the previous kinematic model (Amelung et al., 2000), in which sill opening is constrained only by a Laplacian smoothing constraint, our new approach dramatically reduces the number of degrees of freedom in the inversion.

An approach with a pressure boundary condition is advantageous because the magma pressure is directly relevant to fluid processes in the magma chamber.

In particular, the total magma pressure p_m is the sum of the excess magma pressure Δp and the lithostatic pressure p_L,

$$p_m = \Delta p + p_L. \tag{1}$$

We estimate Δp from the InSAR data. However, it should be noted that the estimated Δp represents only the change in pressure during the time period of the InSAR observations. Assuming a lithostatic stress state, $p_L = \rho\, g\, d$, where ρ is the density of overlying rock, d is the depth of the magma body, measured from the caldera floor. Since the magma chamber is known to be located inside the flat caldera of Sierra Negra at shallow depth (Amelung et al., 2000), we simplify the problem and assume an elastic half-space, ignoring topographically induced stresses (Pinel and Jaupart, 2003). Given the excess magma pressure, we can calculate the stress in the neighborhood of the sill using the pressure as boundary condition. Knowledge of the stress field allows us to consider crack initiation and propagation criteria, since cracks may propagate at roughly constant pressure. Moreover, by calculating stress fields around the magma chamber caused by magma pressurization, we should be able to predict the direction of crack propagation, and thus the evolution of the system. Overall, the new method relates to physical properties of the magma itself, and will better describe the mechanical interaction of the magma intrusion with the surrounding rock.

Later in this paper we find that even with both vertical and horizontal displacement data at the Earth's surface we cannot uniquely determine the shape of the magma chamber. We use the boundary element technique to explore the range of models consistent with the InSAR data, providing clearer constraints on magma chamber geometry.

2 Shape of the Magma Chamber

Non-uniqueness of the shape of subsurface magma chambers (e.g. Dieterich and Decker, 1975) is greatly reduced if both vertical and horizontal deformation data are available (Fialko et al., 2001a). Sills produce little horizontal displacement relative to the peak uplift, as compared to equi-dimensional magma bodies which generate more horizontal deformation. Since imaging radar satellites are side-looking, interferograms record horizontal deformation as well as vertical deformation. Using data from both ascending and descending orbits, it is possible to determine the vertical displacement and one component of horizontal displacement.

Satellites can acquire data when they pass from south to north (ascending) and from north to south (descending). Data from ascending and descending orbits have different imaging geometry (look direction), providing two linearly independent LOS measurements. In principle, we can calculate the 3-D displacement field, using data from both ascending and descending orbits (Fialko et al., 2001b), by solving for three orthogonal components of the surface displacement field from the two LOS displacements and also the interferogram azimuth offsets, which are acquired by cross-correlating two amplitude images. However, in the case of Sierra Negra for the time period when the ascending/descending pair is available, the maximum horizontal surface displacement is less than 10 cm. The accuracy of the azimuth offsets is about 12.5 cm, if we assume that we can measure pixel offsets locally between two images to 1/32 of a pixel (Jónsson et al., 2002). Hence, the signal-to-noise ratio is not sufficient for the azimuth offsets to be meaningful, and we cannot fully reconstruct the 3-D displacement field. Consequently, the vertical com-

ponent and only one horizontal component can be determined. In the case of volcano deformation, assuming near-circular symmetry allows the one component of horizontal displacement to be considered as a radial component. This is adequate since we only need vertical and radial components to reduce the non-uniqueness of the shape of magma chambers.

The ERS-2 data we used are shown in Table 1. Fig. 2 shows a map view of the ascending and descending orbits and the idealized surface displacement vectors due to volcano deformation. Using the same notation as Fialko et al. (2001b), the LOS vector can be expressed in terms of displacements, U_i, as:

$$d_{los} \;=\; [\,U_n \sin\phi \;-\; U_e \cos\phi\,] \sin\lambda \;+\; U_u \cos\lambda, \tag{2}$$

where ϕ is the azimuth of the satellite heading vector (positive clockwise from the North), and λ is the radar incidence angle. Since the orbit inclination of the ERS-2 satellite is 98.5°, which is the angle between the heading vector of the ascending satellite and the easting vector at the equator, the LOS displacement fields contain horizontal components that are off by 8.5° from easting or westing vectors. Thus, the ϕ's for ascending and descending orbits are -8.5° and 188.5° respectively. We approximate these values to 0° and 180°. With this approximation, Eq. 2 reduces to,

$$d_{los} \;=\; \mp U_e \sin\lambda \;+\; U_u \cos\lambda, \tag{3}$$

where the minus sign is for data from ascending orbit and the plus sign is for data from descending orbit. Since there are two unknowns and two equations we can solve for U_u and U_e. We verify the accuracy of this approximation by reconstructing the vertical and radial components from a well known

circularly symmetric deformation source. Fig. 3 shows the true vertical and radial components due to the Mogi point source (Mogi, 1958) and the reconstructed components, derived from simulated interferograms from ascending and descending orbits using the ERS-2 satellite's actual orbit inclination. The interferograms were transformed into vertical and easting components. The approximation-induced error is about 1% in this case.

The actual ascending and descending interferograms and the reconstructed vertical and horizontal components are shown in Fig. 4. The interferograms have been processed using the Jet Propulsion Laboratory/Caltech repeat orbit interferometry package ROI_PAC. A 90-meter posting Digital Elevation Model (DEM) from the Shuttle Radar Topography Mission (SRTM) was used to subtract the topographic signal. Note that neither the vertical nor the easting component is perfectly symmetric, implying a lack of symmetry in the deformation source. In order to check the effect of this asymmetry, we implemented a simulation which reconstructed the east component of displacement for different orientations of the deformation source (Fig. 5). We rotated the best-fit model, which will be described in the inversion section, and reconstructed the east component from the rotated models. This figure shows how far the model is from circular symmetry. Specifically, each subfigure demonstrates the symmetry about N-S axis through the center of the image. Note that a 60° model rotation shows the best symmetry about N-S axis, implying that the deformation source has an axis of symmetry whose strike is about 60° from the north. This axis of symmetry can also be seen in the vertical component (Fig. 4c).

Fig. 6 shows the profiles of vertical and east components along A-A' in Fig. 4d. The line A-A' was chosen so that it includes both the maximum vertical

displacement and maximum horizontal displacement. The ratio of the maximum horizontal to maximum vertical displacement is about 0.3, consistent with a sill, but inconsistent with a spherical (Mogi) source for which the ratio is about 0.4 (Fialko et al., 2001a). Thus, this observation supports the idea that the magma reservoir beneath Sierra Negra is a sill, or a sill-like body.

3 Estimation of Best-fitting Sill Geometry

We determined the sill geometry using a 3-D boundary element method plus a non-linear inversion scheme. In this approach, the geometry of the sill is described by its periphery or fracture tip-line and its depth. We used the same SAR scenes (1998/09/26 and 1999/03/20) that Amelung et al. (2000) used to form an interferogram, rather than the ascending and descending pair used in the previous section (Table 1), to facilitate comparison of our results with the kinematic model of Amelung et al. (2000). The deformation pattern in the previous section (Fig. 4a,b) is similar in shape to the interferogram used for modeling (Fig. 10a) but smaller in amplitude. We compared the two interferograms by scaling the one for inversion ($\mathbf{s}_1$) to fit the one in the previous section ($\mathbf{s}_2$). To do this we estimate a scale factor a and phase offset b minimizing,

$$\min_{a,\,b} ||\mathbf{y} - (a\,\mathbf{x} + b)||_2, \tag{4}$$

The phase offset b is necessary because the two interferograms do not share a master image. Fig. 7 shows that the surface deformation is nearly identical and implies that the deformation sources in the two time periods share the same geometry. Thus, the only difference between the two time periods should

be the magnitude of the excess magma pressure. In general, if the deformation pattern is the same in a number of interferograms, we can fix the geometry of the deformation source by modeling only one of the interferograms. For this reason, we can now model the deformation source using the third interferogram (Table 1), starting from the result of the previous section; that is, the deformation source is a sill.

3.1 Forward Modeling

We assume that uniform pressure acts everywhere on the surface of the sill, with no shear traction. A uniform pressure boundary condition is physically more reasonable than a kinematic displacement boundary condition, because Sierra Negra commonly erupts low viscosity basaltic magma which should be close to hydrostatic pressure equilibrium.

We divide the crack into elements that either opened or remained closed in order to determine the sill geometry. The uniform pressure boundary condition is enforced on all open elements. Various combinations of open and closed elements are selected to form a sill. Once a candidate sill periphery, depth, and uniform pressure are selected, the opening distribution of the entire sill is uniquely determined by a boundary element calculation. This reduces the number of degrees of freedom of the boundary value problem relative to the kinematic inversion.

We wish to use the boundary value problem as the forward function in an inversion, therefore we introduce a set of binary parameters describing whether each element in a grid is open or closed. Fig. 8 shows a simple example of

a model grid. A value of zero at a grid cell means that the sill element is closed (i.e. not a part of the sill) and a "one" means that the sill element is open. Only the open elements are subject to the uniform internal pressure condition. Determining the geometry of the sill is equivalent to determining the appropriate combination of zeros and ones.

We choose depth, excess magma pressure, and one combination of the binary parameters. These suffice to determine the opening distribution in the entire model grid uniquely, using a 3-D boundary element calculation. Surface deformation is then derived from the sill opening using Green's functions integrated over a rectangular element in an isotropic homogeneous linear elastic half-space (e.g. Okada, 1992). The shear modulus of the elastic half-space was assumed to be 30 GPa, and 0.25 was assumed for Poisson's ratio. Since the InSAR data are sensitive only to the ratio of the excess magma pressure to the shear modulus, decreasing the shear modulus by a factor of 3, would decrease the estimated excess magma pressure by the same factor.

3.2 Nonlinear Inversion

Once the forward methodology is defined, we can proceed to select the best-fit model through inversion. The goal here is to estimate the best-fitting sill geometry, excess magma pressure, and depth. The binary nature of the crack opening makes the problem highly nonlinear. In this case, the misfit or objective function is not quadratic, thus convergence to the global minimum is not guaranteed. Moreover, binary parameters are discrete and thus not differentiable. Therefore a gradient-based inversion scheme is not possible. As our model grid size is 16 by 18, the number of possible combination of the binary

parameters is 2^{288}. Because it is infeasible to test all possibilities, we employed simulated annealing, a stochastic nonlinear inversion scheme (Metropolis et al., 1953).

Simulated annealing was proven to converge with an infinite number of iterations at a constant (metaphorical) temperature parameter (Rothman, 1986). The cooling schedule is important as it determines whether the global minimum can be achieved or not, and it also affects the speed of convergence. We use a simulated annealing code (Cervelli et al., 2001) that applies Basu and Frazer type rapid determination of critical temperature (Basu and Frazer, 1990). For sampling at each temperature we use the heat bath algorithm, where one parameter is perturbed at one iteration while the others are fixed. The code was modified to accommodate the binary parameters.

The data vector in our inversion is the observed LOS displacements $\mathbf{d}_{los}$. The size of the original InSAR data set (16384 pixels) was reduced to 674 points using quadtree partitioning (Jónsson et al., 2002) to make the problem manageable. The model vector $\mathbf{m}$ contains the set of binary parameters and the excess magma pressure Δp. Thus,

$$\mathbf{d}_{los} \;=\; g(\mathbf{m}) \;+\; \varepsilon, \tag{5}$$

where ε is data error plus errors in the forward model, and the function g includes the dislocation model and the LOS projection of the surface displacement. We adopt an L_2 objective function,

$$\Phi \;=\; ||\,\mathbf{d} \;-\; g(\mathbf{m})\,||_2. \tag{6}$$

The other dislocation model parameters were fixed in the sill plane. The depth

of the sill was estimated by examining the residual pattern as well as the L2-norm of the residual at depths ranging from 1 km to 3 km in 100 m depth increments.

Solutions with isolated individual open elements require physically unrealistic magma pressure (hundreds of MPa). In order to preclude this from our models, we put an upper bound on the excess magma pressure. If a certain choice of geometry yields a magma pressure that is greater than the upper bound, then the candidate geometry is rejected.

We used physical reasoning to derive an initial value for the upper bound on melt pressure. Fig. 9 shows a simplified vertical cross-section containing the magma chamber. Assuming the magma pressure is at equilibrium at depth D, the pressure in the magma chamber p_m propagated through the melt column can be written as,

$$p_m \;=\; \rho_s\, g\, D \;-\; \rho_m\, g\,(h \;+\; D \;-\; d) \tag{7}$$

where ρ_s is the density of solid rock, and ρ_m is the melt density. The excess magma pressure can then be calculated by subtracting the lithostatic pressure due to the overloading rock:

$$\Delta p \;=\; p_m \;-\; \rho_s\, g\, d. \tag{8}$$

For example, if we take $\rho_s = 2.9\,\mathrm{g\,cm^{-3}}$ (Hill and Zucca, 1987), $\rho_m = 2.6\,\mathrm{g\,cm^{-3}}$ (Savage, 1984), $h = 2.4$ km, $D = 37$ km, and $d = 2$ km, we compute an excess magma pressure of 7.6 MPa. Here the h was derived from the difference between the altitude of Sierra Negra's caldera and the average altitude of a circular region about 100 km in radius, centered at Sierra Negra. The thickness of

the lithosphere D was calculated using the thermal diffusivity $\kappa = 1\,\mathrm{mm}^2\,s^{-1}$ (Turcotte and Schubert, 2002) and the age of the lithosphere $t = 8$ Myr (Sallares and Charvis, 2003) in the following equation (Turcotte and Schubert, 2002),

$$D = 2.32\sqrt{\kappa\,t}. \tag{9}$$

Starting from the initial value of excess magma pressure, several choices of the upper bound on excess magma pressure were tested for each depth, and we selected the one that produced reasonable connectivity and the best fit.

Fig. 10 shows the interferogram used for modeling in this part of the study and the best-fit model derived from simulated annealing. An upper bound of 5 MPa was placed on the excess magma pressure. Although disconnected and isolated open elements were effectively suppressed by the upper bound, a few isolated segments remained. Eliminating these did not change the fit to the data significantly because the isolated segments open very little given the estimated excess magma pressure. The best-fitting model after removing the isolated segments is shown in Fig. 11b, in comparison to Amelung et al.'s best-fitting kinematic model (Fig. 11a). Note that the estimated sill is restricted to the inner caldera and is bounded by the sinuous ridge. The depth and excess magma pressure are estimated as 1.9 km and 4.5 MPa respectively. The colors of the sill elements represent the inferred opening distribution, with the maximum being 0.5 m. The total volume change is calculated as 6.7 million cubic meters. If we attribute this volume change to magma influx, the average magma filling rate is about 1.1 million cubic meters per month for the time period 1998/09/26 to 1999/03/20. The overall distribution of estimated sill opening is in good agreement with Amelung et al.'s kinematic model as

expected.

4 Discussion

In this section we further explore the non-uniqueness of the shape of the magma chamber. Although an equi-dimensional magma chamber or stock was rejected previously, our analysis does not prove that the source of deformation is a thin sill. If the radius of the sill is large compared to the depth, the surface deformation is dominated by displacement of the sill's upper surface. We thus suspect that surface deformation would be insensitive to the sides and bottom of the chamber.

We test this using a boundary element code, Poly3D (Thomas, 1993). The Poly3D superposes the solution for an angular dislocation (Yoffe, 1960; Comninou and Dundurs, 1975) to calculate the displacements, strains, and stresses induced in an elastic whole- or half-space by planar polygonal elements of displacement discontinuity and boundary element method. Fig. 12 shows the geometry of a flat-topped diapir used in this test. The depth to the top is 1.9 km, and the radius of the top is 3 km, resembling the estimated geometry of the sill at Sierra Negra. The sides of the diapir are dipping inward at an angle of 45°. The lower part of the diapir has a hole, whose radius is 600 m. This is done to avoid numerical instability due to rotation of the inner region with respect to the outer region. The surface deformation is compared to the surface deformation due to a circular disk or a sill. The geometry of the sill is simply the top part of the diapir. From Fig. 12 it is clear that flat-topped diapirs produce almost identical surface deformation to sills, as long as the depth is small compared to the radius. Thus, while we have greatly narrowed

the class of viable magma chamber shapes, the deformation data alone cannot uniquely resolve this question.

To differentiate between the two models, we consider thermal interaction of the intruded magma body with the host rock. If we consider a single intrusion event, the time required for complete solidification of the sill can be calculated by,

$$t_s = \frac{b^2}{4\,\kappa\,\lambda_2^2}, \tag{10}$$

where b is the half-width of a sill of uniform thickness and λ_2 is a dimensionless variable defined as $\lambda_2 = y_m/(2\sqrt{\kappa t})$, where y_m is the distance from the boundary between the sill and the country rock to the solidification boundary within the sill. The variable λ_2 is numerically determined from the following transcendental equation,

$$\frac{L\sqrt{\pi}}{c(T_m - T_0)} = \frac{e^{-\lambda_2^2}}{\lambda_2(1\ +\ erf\,\lambda_2)}, \tag{11}$$

where L is the latent heat of fusion, c is the specific heat, and T_m and T_0 are melt temperature and the initial wall rock temperature (Turcotte and Schubert, 2002). Taking $L = 320\,\mathrm{kJ\,kg^{-1}}$, $T_m - T_0 = 1000$ K, $c = 1.2\,\mathrm{kJkg^{-1}K^{-1}}$, we get $\lambda_2 = 0.73$. Then with $\kappa = 1\,\mathrm{mm^2s^{-1}}$ and the thickness of the sill of 0.5 m ($b = 0.25$ m), the time required for this intrusion to completely solidify is about 8 hours (Turcotte and Schubert, 2002). Considering that 0.5 m was the maximum opening, the intruded sill would have solidified even faster.

The uplift observed at Sierra Negra by InSAR data since 1992 has shown a consistent spatial pattern for several years except when there was trapdoor faulting. In particular, the pattern prior to and after the trapdoor faulting was

very similar (Amelung et al., 2000). Therefore, it is unlikely that numerous thin sills intruded and solidified during this time period. If separate sills intruded and solidified, there would be no particular reason that they would each produce the same surface deformation pattern. Instead, it is more likely that a thicker continuously liquid magma chamber experienced pressure increases, or equivalently volume increases, which in turn produced the surface deformation. If this was the case, we can conversely calculate the minimum thickness of the magma chamber for it to have remained liquid over the time period of observation. Taking $t_s = 7$ yrs in Eq. 10, b is calculated to be approximately 20 m, and thus the minimum thickness is about 40 m.

Another way to distinguish between different magma chamber geometries, is to consider the perturbation in the stress field due to magmatic intrusions. Although the surface displacement fields due to a sill and a diapir are not distinguishable, the stress fields generated by the two different magma bodies are different. The stress state is difficult to measure directly. However, the orientation of fissure eruptions on the flank of Sierra Negra is an important clue to the stress field, since dikes and sills are known to propagate perpendicular to the least compressional principal stress. Interestingly Chadwick and Dieterich (1995), who compared stress directions with the orientations of dikes on Sierra Negra, favor a flat-topped diapir, equivalent to one of the models we find to be consistent with the InSAR data.

5 Conclusions

We have narrowed the class of candidate models consistent with the InSAR observations of Sierra Negra. We have shown the data require a flat-topped

magma body at a depth of about 2 km restricted to the inner caldera. Deformation data alone, however, cannot uniquely determine the geometry of the sides or feeder conduit – both a diapir and a sill with uniform internal pressure provide reasonable fits to the data. The InSAR data do constrain the lateral geometry of the magma chamber to a high resolution.

We solved for the shape of the sill, or equivalently the flat top of the diapir. A physically reasonable uniform pressure boundary condition was used in the inversion. The estimated sill opening was similar to that estimated by Amelung et al. (2000). Fitting the data equally well with reduced number of degrees of freedom suggests that the physical constraint used in this study was reasonable. It gives physical insight to conditions in and around the magma chamber. The estimated excess magma pressure can be used to infer the stress field in the surrounding rock. This will be useful for estimating the crack propagation criteria and predicting the direction of crack propagation, which may lead to an eruption.

The technique that uses data from ascending and descending orbits to resolve the shape of magma chambers can be applied to any type of deformation source particularly those with radial symmetry. The binary-parameter inversion scheme used to resolve the detailed geometry of the sill can be applied to any type of uniform pressure planar deformation source.

6 Acknowledgments

We thank Falk Amelung for providing ERS-2 data that helped to make ascending/descending pair. The manuscript was greatly improved by construc-

tive and thoughtful comments from Dennis Geist and Joachim Gottsman. This work was supported by Korean Overseas Scholarship and NSF grant EAR-0001096.

References

Amelung, F., Jónsson, S., Zebker, H., Segall, P., 2000. Widespread uplift and 'trapdoor' faulting on galapagos volcanoes observed with radar interferometry. Nature 407 (6807), 993 – 6.

Basu, A., Frazer, L. N., 1990. Rapid determination of the critical temperature in simulated annealing inversion. Science 249 (4975), 1409 – 12.

Cervelli, P., Murray, M. H., Segall, P., Aoki, Y., Kato, T., 2001. Estimating source parameters from deformation data, with an application to the march 1997 earthquake swarm off the izu peninsula, japan. Journal of Geophysical Research 106 (B6), 11217 – 37.

Chadwick, W., Dieterich, J., 1995. Mechanical modeling of circumferential and radial dike intrusion on galapagos volcanoes. J. Geophys. Res. 66 (1-4), 37 – 52.

Comninou, M., Dundurs, J., 1975. The angular dislocations in a half space. Journal of Elasticity 5 (3/4), 203 – 16.

Dieterich, J., Decker, R., 1975. Finite element modeling of the surface deformation associated with volcanism. J. Geophys. Res. 80.

Fialko, Y., Khazan, Y., Simons, M., 2001a. Deformation due to a pressurized horizontal circular crack in an elastic half-space, with applications to volcano geodesy. Geophysical Journal International 146 (1), 181 – 90.

Fialko, Y., Simons, M., Agnew, D., 2001b. The complete (3-d) surface displacement field in the epicentral area of the 1999 msub w7.1 hector mine

earthquake, california, from space geodetic observations. Geophysical Research Letters 28 (16), 3063 – 6.

Geist, D., Chadwick, W., Johnson, D., in review 2004. Results from new gps and gravity monitoring networks at fernandina and sierra negra volcanoes, galapagos, 2000-2002. Journal of Volcanology and Geothermal Research.

Hill, D. P., Zucca, J. J., 1987. Geophysical constraints on the structure of kilauea and mauna loa volcanoes and some implications for seismomagnetic processes. Volcanism in Hawaii 2, 903 – 917.

Jónsson, S., Zebker, H., Amelung, F., in review 2004. On trapdoor faulting at sierra negra volcano, galápagos. Journal of Volcanology and Geothermal Research.

Jónsson, S., Zebker, H., Segall, P., Amelung, F., 2002. Fault slip distribution of the 1999 msub w 7.1 hector mine, california, earthquake, estimated from satellite radar and gps measurements. Bulletin of the Seismological Society of America 92 (4), 1377 – 89.

Metropolis, N., Rosenbluth, A. W., Rosenbluth, M. N., Teller, A. H., Teller, E., 1953. Equation of state calculations by fast computing machines. Journal of Chemical Physics 21 (6), 1087 – 1092.

Mogi, K., 1958. Relations between the eruptions of various volcanoes and the deformations of the ground surfaces around them. Bull. Earthquake Res. Inst. Univ. Tokyo 36, 111–123.

Munro, D. C., Rowland, S. K., 1996. Caldera morphology in the western galapagos and implications for volcano eruptive behavior and mechanisms of caldera formation. Journal of Volcanology and Geothermal Research 72 (1-2), 85 – 100.

Okada, Y., 1992. Internal deformation due to shear and tensile faults in a half-space. Bulletin of the Seismological Society of America 82 (2), 1018 –

40.

Pinel, V., Jaupart, C., 2003. Magma chamber behavior beneath a volcanic edifice - art. no. 2072. Journal of Gephysical Research-Solid Earth 108 (B2), 2072 – 2072.

Reynolds, R. W., Geist, D., Kurz, M. D., 1995. Physical volcanology and structural development of sierra negra volcano, isabela island, galapagos archipelago. Geological Society of America Bulletin 107 (12), 1398 – 1410.

Rothman, D. H., 1986. Automatic estimation of large residual statics corrections. Geophysics 51 (2), 332 – 46.

Sallares, V., Charvis, P., 2003. Crustal thickness constraints on the geodynamic evolution of the galapagos volcanic province. Earth and Planetary Science Letters 214 (3-4), 545 – 559.

Savage, J. C., 1984. Local gravity-anomalies produced by dislocation sources. Journal of Geophysical Research 89 (NB3), 1945 – 1952.

Thomas, A. L., 1993. Poly3d: A three-dimensional, polygonal element, displacement discontinuity boundary element computer program with applications to fractures, faults, and cavities in the earth's crust. M.S. Thesis, Stanford University, Department of Geological and Environmental Sciences, Stanford, CA.

Turcotte, D. L., Schubert, G., 2002. Geodynamics, 2nd Edition. Cambridge University Press, Cambridge, UK.

Yoffe, E. H., 1960. The angular dislocation. Philosophical Magazine 5 (50), 161 – 175.

Table 1

Interferograms Used in This Study

Orbit direction	Scene 1	Scene 2	$T_\perp$	$B_\perp$
Ascending	1998/10/31	1999/02/13	3.5 months	152 m
Descending	1998/11/05	1999/02/18	3.5 months	448 m
Ascending	1998/09/26	1999/03/20	6 months	50 m

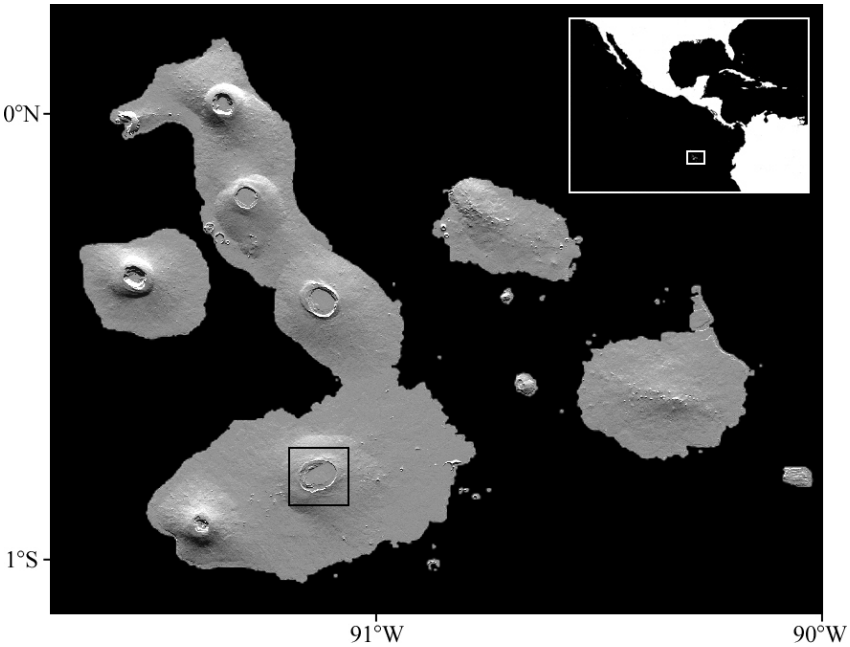

Fig. 1. Shaded relief topographic map of Galápagos Islands. The study area is indicated with a black box, which includes the caldera of Sierra Negra volcano.

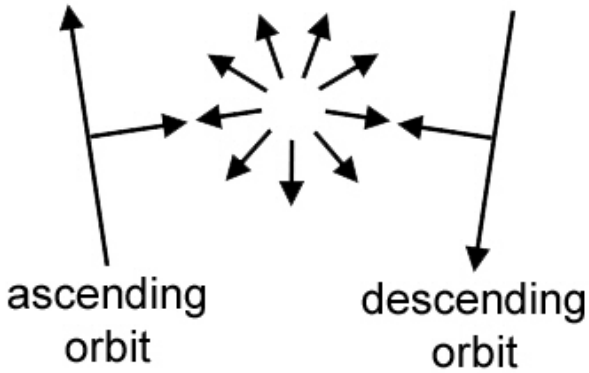

Fig. 2. Map view of ascending and descending orbit imaging geometry and idealized surface displacement of volcano deformation.

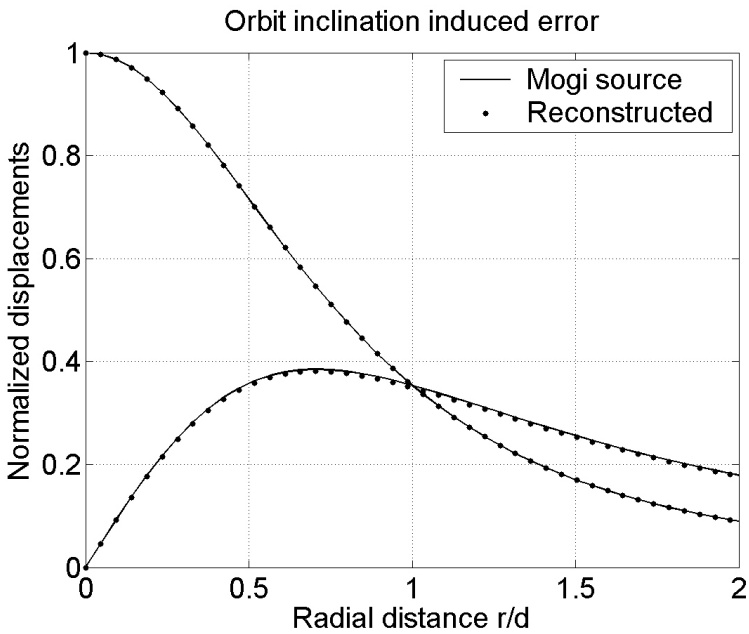

Fig. 3. Circularly symmetric deformation source was used to estimate the satellite orbit inclination induced error. The vertical and radial component are reconstructed in the same way as the data was analyzed. In the case of circular symmetry, the maximum error due to the orbit inclination not being 90° is about 1%.

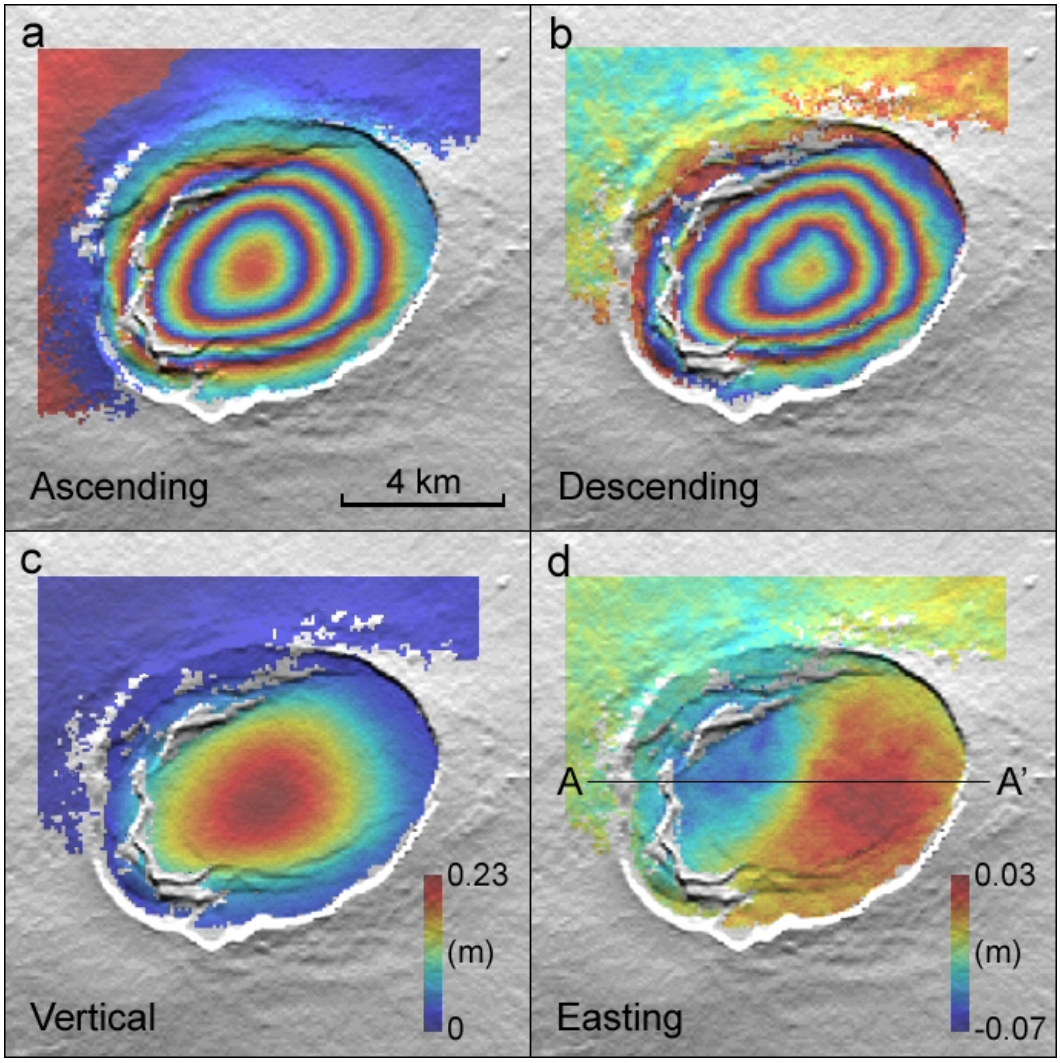

Fig. 4. Interferograms from ascending (a) and descending (b) orbits with temporal baselines of 1998/10/31 - 1999/02/13 and 1998/11/05 - 1999/02/18 respectively. One color cycle represents 5 cm change of range in LOS direction of satellite. Interferometric displacements can be separated into vertical (c) and horizontal (d) components using the imaging geometries of the two orbits.

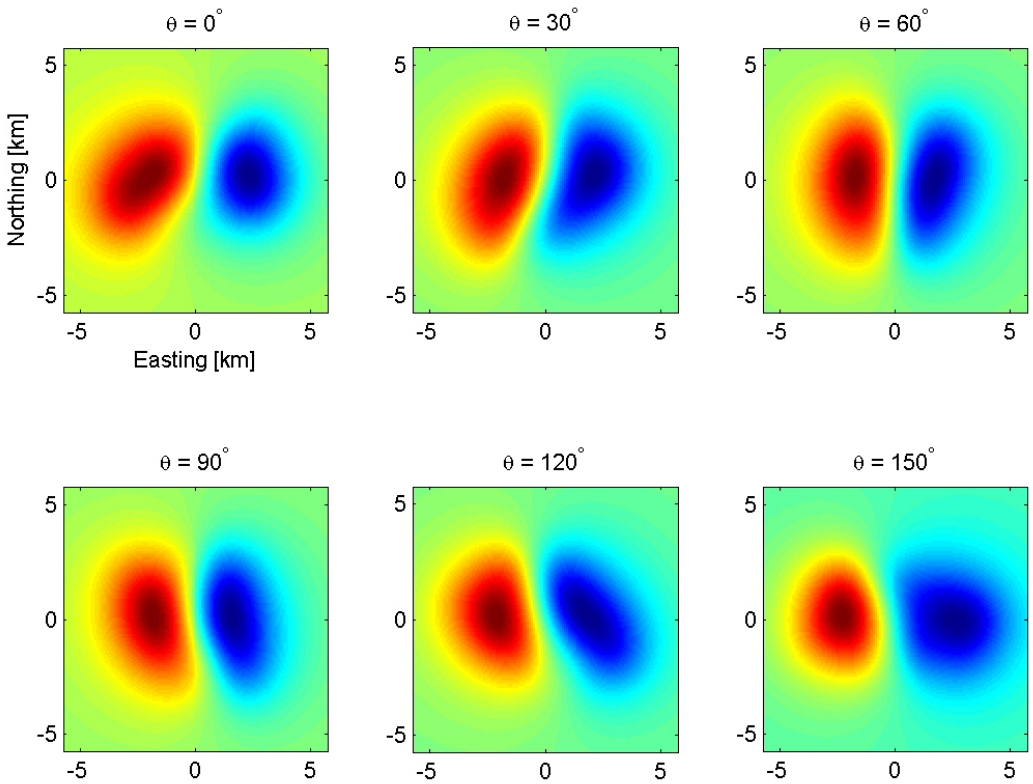

Fig. 5. Asymmetry test using the best-fit model. The best-fit model was rotated from 0° to 150° in 30° increments. θ is the angle of counterclockwise rotation. At each angle two interferograms from ascending and descending orbit were simulated, and it was transformed into east component as described in section 2.

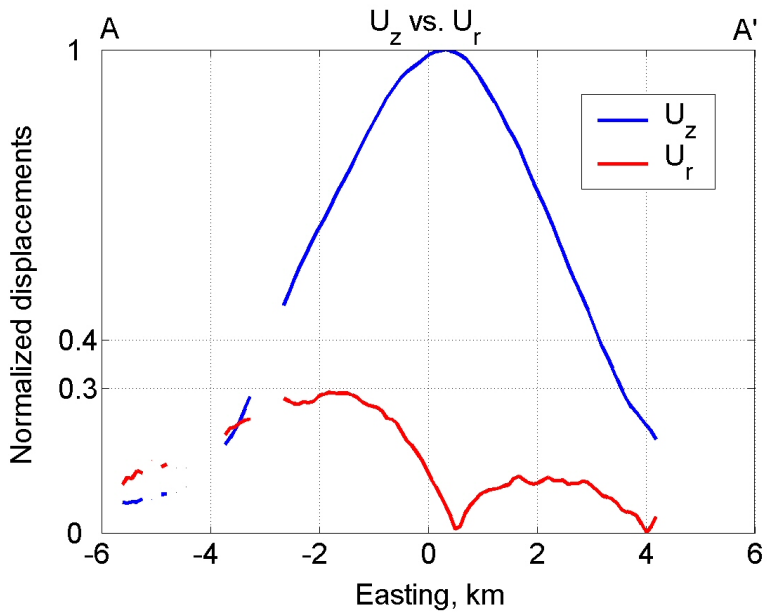

Fig. 6. Profile along A-A' in Fig. 4d. Five lines were averaged to produce smooth plot. Absolute value of east component is plotted to represent radial component.

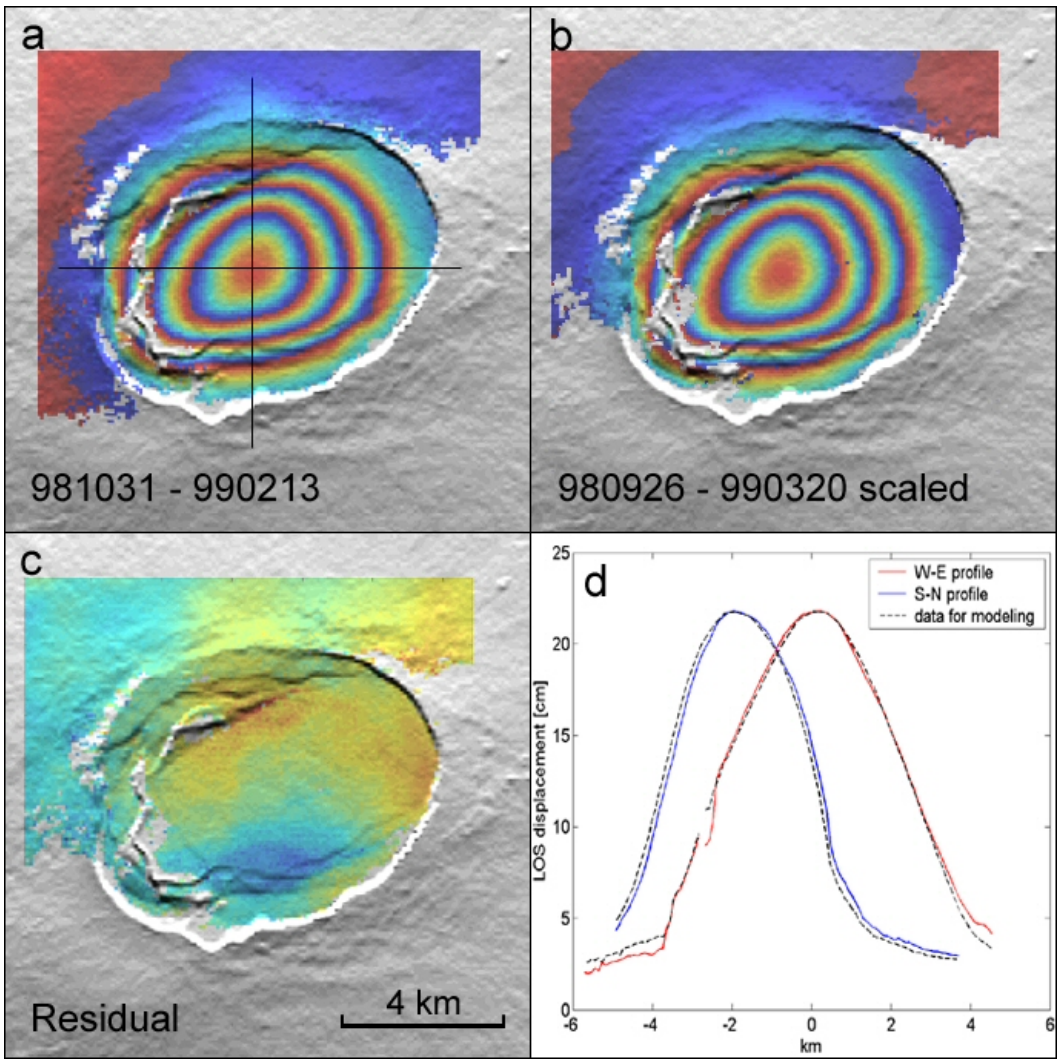

Fig. 7. Least-squares fitting results. (a) Interferogram for the time period of 1998/10/31 - 1999/02/13. (b) Scaled version of the the interferogram for 1998/09/26 - 1999/03/20. (c) Residual. (d) Profiles through (a) and (b). The blue solid line is the S-N profile of (a), and the red solid line is the W-E profile of (a). The black dashed lines are the corresponding profiles of (b). One color cycle in the interferograms and residual represents 5 cm of LOS displacement.

0	0	0	0	0
0	0	1	1	0
0	0	0	1	0
0	1	0	0	0
0	0	0	0	0

Fig. 8. Simple example of model grid that shows four open sill elements. The upper right corner sill element will open widest under uniform pressure.

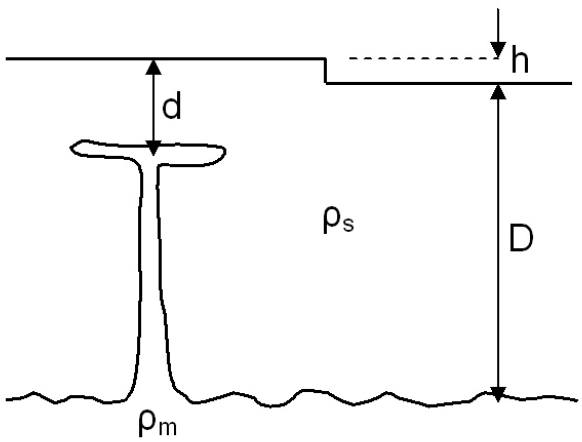

Fig. 9. Schematic vertical section of the lithosphere.

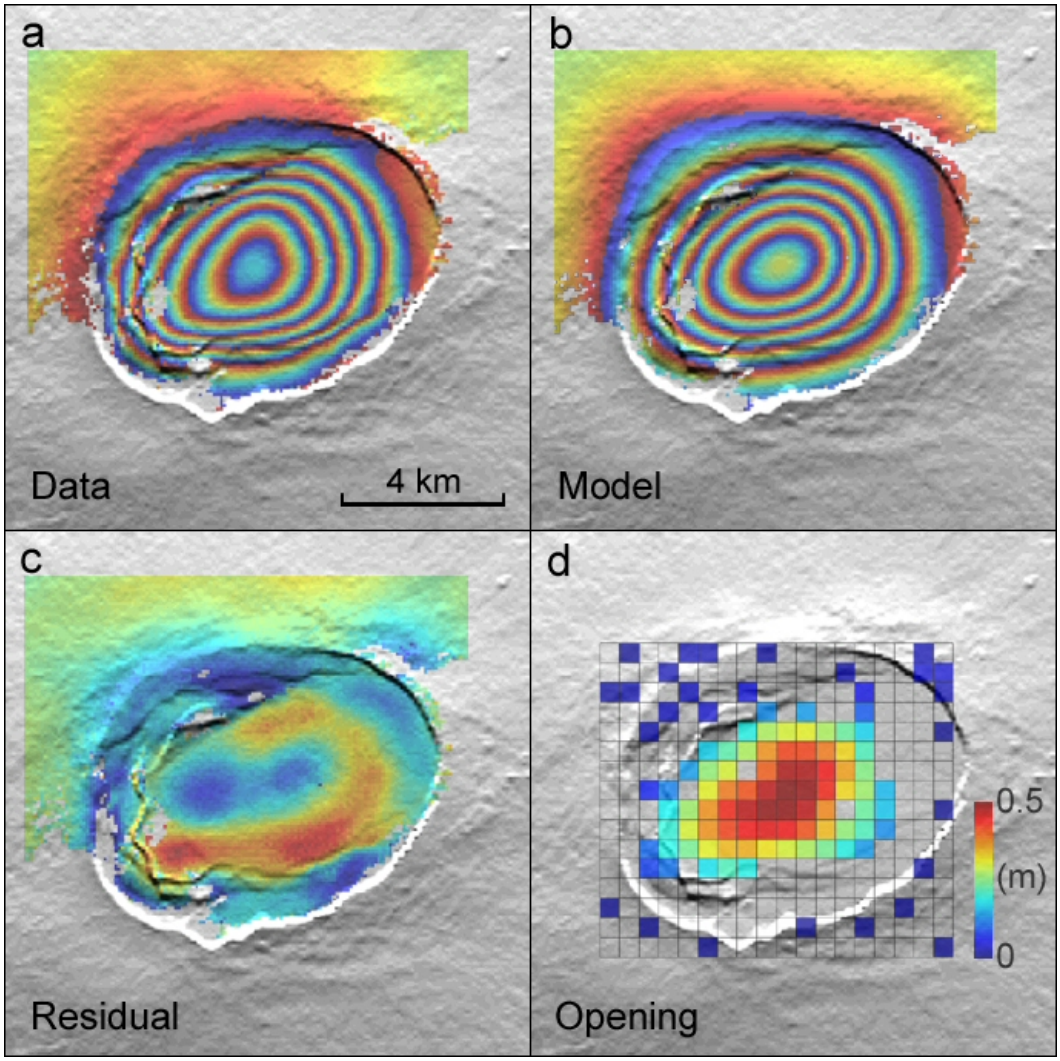

Fig. 10. Observed interferogram (a) and simulated interferogram (b) from the best-fit model (d). The residual (c) between the data and the model shows differences smaller than 2.5 cm, half the magnitude of one color cycle in (a) and (b).

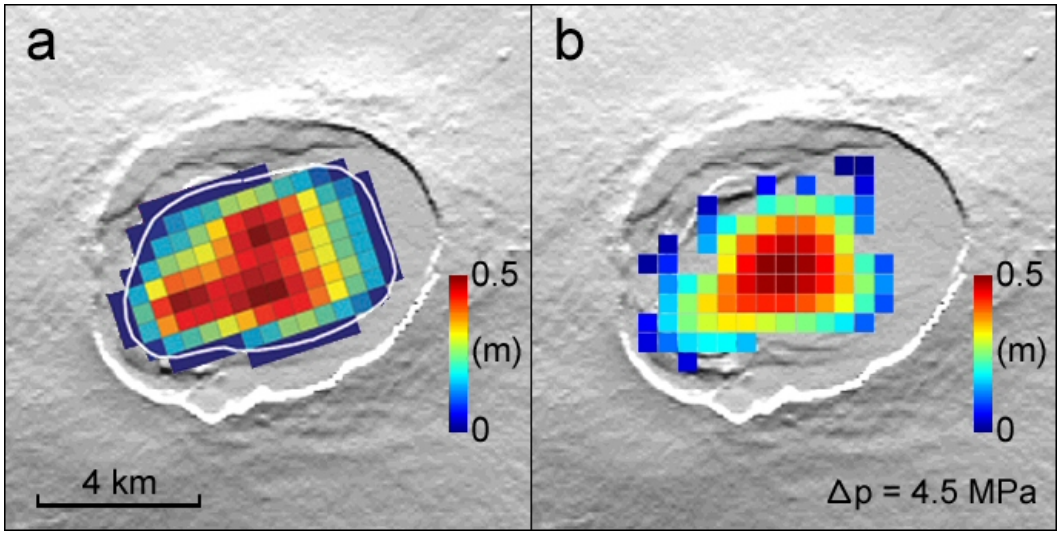

Fig. 11. (a) Best-fit model of Amelung et al. using a sill model with spatially varying opening distribution. (b) Best-fit model with uniform pressure boundary condition. Depth was estimated as 1.9 km in both cases.

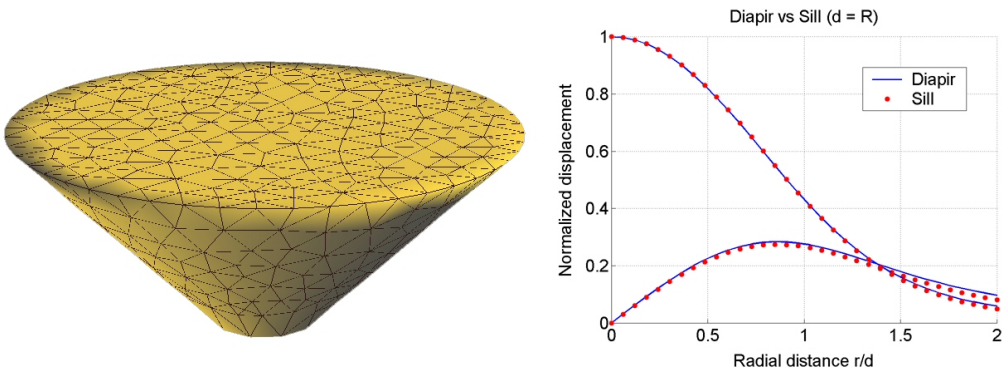

Fig. 12. (a) A flat-topped diapir with its sides dipping 45°. The depth to the top of the diapir is d, and the radius of the top of the diapir is R. (b) Surface deformation due to the diapir and a sill whose geometry is the same as the top of the diapir. The line of observation points are located on the surface of the half-space starting from directly above the center of the diapir. The x-axis is the distance normalized by the radius, and the y-axis is displacement normalized by the maximum vertical displacement.